

# Large Pyroelectric Enhancement in Freestanding Epitaxial BaTiO<sub>3</sub> Membranes on Si

Ajay Kumar\*#, Asraful Haque\*#, Shubham Kumar Parate, Harshal D'Souza, Jishnu NK, Binoy Krishna De, Srinivasan Raghavan, Pavan Nukala\*

Centre for Nano Science and Engineering, Indian Institute of Science, Bangalore 560012, India

# equal contribution

## Abstract

Ferroelectric membranes transferred onto arbitrary substrates provide reduced mechanical clamping at the interfaces that can diminish the effective polarization-rotation barrier offering a pathway to engineer larger electromechanical and thermally driven responses in oxide electronics. Here, we report integration of single crystalline thin film BaTiO<sub>3</sub> (BTO) ferroelectric membrane on Si and demonstrate a 4× at 30°C and 34× at 60°C enhancement of pyroelectric coefficient compared to clamped films. The BTO membrane is grown epitaxially on a water-soluble Sr<sub>3</sub>Al<sub>2</sub>O<sub>6</sub> sacrificial layer, released by selective dissolution, and transferred onto Si, yielding a strain-relaxed membrane with robust intrinsic polarization. Temperature-dependent piezoresponse force microscopy (PFM) reveals pronounced thermally driven evolution of domain orientation, consistent with reduced barriers for dipolar modulation in the freestanding state. Variable-temperature Kelvin probe force microscopy (KPFM) quantifies an effective pyroelectric coefficient of ~75 μC/m<sup>2</sup>K at 30°C and 450 μC/m<sup>2</sup>K at 60°C with a detectivity of 40 m<sup>2</sup>K<sup>-1</sup> at room temperature. These results establish lead-free freestanding BTO membranes as a promising silicon-integrable platform for cryogen-free infrared detection and waste-heat energy management.

Keywords: Free-standing oxide membrane, Pyroelectricity, Ferroelectricity, strain-engineering, Heterogeneous integration on Si, BaTiO<sub>3</sub>.

Single-crystalline freestanding oxide membranes have emerged as a powerful platforms that decouple epitaxial quality of the films from the constraints of the growth substrate, enabling integration of complex oxides onto arbitrary surfaces.<sup>1,2,3,4</sup> Epitaxial integration onto Si has traditionally relied on monolithic oxide-on-Si growth using complex multilayer buffer or template stacks; such as Sr-passivated SrTiO<sub>3</sub>/Si or LNO/CeO<sub>2</sub>/YSZ/Si architectures to mitigate challenges associated with native SiO<sub>x</sub> formation, reactive interfacial chemistry, and large lattice and thermal-expansion mismatches.<sup>5,6</sup> By comparison, membrane release and transfer preserves single-crystal order while enabling integration on Si with simplified interfacial design. Among the most widely used routes to freestanding oxides are sacrificial-layer lift-off/transfer and remote epitaxy-enabled exfoliation.<sup>7,8,9,10</sup>

Beyond (Si) integration, ferroic freestanding membranes are less elastically constrained by interfaces, reducing the clamping effects seen in monolithically grown thin-films. The release of substrate clamping and the creation of free surfaces can flatten the free-energy landscape (Figure 1a) and unlock highly mobile domain walls and unconventional domain topologies.<sup>11</sup> Recent theoretical and experimental studies have shown that reduced elastic constraints and altered lattice dynamics in freestanding ferroelectrics can promote low-energy polarization rotation pathways and dynamic domain responses that are difficult to access in conventional clamped thin films.<sup>13</sup> In extreme cases, strain-engineered topological/domain textures (e.g., helical dipolar structures in ferroelectric membranes) were shown to activate rotational soft modes and yield anomalously large electromechanical responses compared to single-domain states.<sup>11</sup>

These same boundary-condition changes are also expected to strongly impact pyroelectricity, where a temporal temperature change modulates spontaneous polarization. Pyroelectric materials are central to uncooled infrared (IR) detection<sup>14</sup>, thermal imaging<sup>15</sup>, and waste-heat energy harvesting<sup>16</sup>, where maximizing the pyroelectric coefficient and relevant figures of merit is crucial for high responsivity and detectivity. In classical form, the pyroelectric coefficient can be expressed as  $p = (\partial P_s / \partial T)_\sigma$ , with contributions that are often separated into (a) primary pyroelectricity (intrinsic polarization change in a clamped lattice) and (b) secondary pyroelectricity (polarization change mediated by thermally induced strain through piezoelectric coupling).<sup>17</sup> In thin-film pyroelectrics on rigid substrates, substrate clamping and thermal-expansion mismatch can suppress or complicate these contributions, motivating approaches that directly modify mechanical boundary conditions.<sup>18</sup>

*Zhang et al.* reported record high pyroelectricity of  $1.76 \times 10^{-2} \text{ C m}^{-2} \text{ K}^{-1}$  in 10 nm atomically flat PMN-PT freestanding membranes, which increases sharply with decreasing thickness.<sup>19,20</sup> While such large pyroelectric coefficients are attributed to ultrathin and unclamped nature of the films, and is highly attractive for cryogen-free infrared detection, the microscopic mechanism remains unclear.

Recent studies have shown that ferroelastic and mechanically deformed mobile domain walls can actively enhance pyroelectricity.<sup>21,22</sup> These effects, combined with the absence of clamping strain and presence of switchable, mobile domains, provide an opportunity to systematically investigate the role of thermally driven polarization dynamics in pyroelectricity with a model system. Single-crystalline BaTiO<sub>3</sub> (BTO) membranes a prototypical lead-free ferroelectric material characterized by mobile ferroelastic domains and facile domain reorientation, provide a simplified and well-controlled platform to elucidate the governing mechanisms.<sup>23-27</sup> However, prior investigations of pyroelectricity in BTO have primarily focused on epitaxial films on oxide substrates, polycrystalline films on Si (both substrate-clamped and self-supported), and bulk single crystals, leaving the behavior of freestanding-BTO (FS-BTO) comparatively unexplored.<sup>22, 28-30</sup>

Here, we integrate single-crystalline epitaxial BaTiO<sub>3</sub> membranes onto CMOS-compatible substrate, i.e., silicon and demonstrate robust, strongly enhanced pyroelectricity enabled by strain relaxation and thermally responsive ferroelastic domain dynamics. Mechanistic insight into the origin of pyroelectricity is provided by temperature-dependent piezoresponse force microscopy, which reveals pronounced thermally driven domain reconfiguration in the freestanding state. Meanwhile, variable-temperature Kelvin probe force microscopy quantitatively resolves an effective pyroelectric coefficient approximately four times higher at 30°C and thirty-four times higher at 60°C than that of substrate-clamped thin-film controls. These results establish lead-free, silicon-integrable BaTiO<sub>3</sub> membranes as promising materials platform for cryogen-free infrared detection and on-chip thermal sensing, while providing insights into declamping-driven pyroelectricity enhancement.

## **Results:**

Epitaxial BTO films were grown on SrTiO<sub>3</sub> (STO) (001) substrate with SAO water soluble sacrificial buffer layer using pulsed laser deposition, as described in Methods section.<sup>31</sup> The heterostructures were then coated with a polymer support, and the SAO layer was selectively dissolved in water to release the membrane and enable transfer of FS-BTO onto a Si substrate (schematic in Figure 1b). High-resolution X-ray diffraction (Figure 1c(i-ii)) of the as-grown BTO/SAO//STO stack and the transferred BTO/Si membrane shows that the (00*l*) Bragg reflections are preserved after transfer, confirming retention of the crystalline order in the transferred membrane (Figure S1). The de-clamping effect shifts the BTO (002) diffraction peak from 44.10° in C-BTO to 44.18° in FS-BTO, indicating an out of plane strain relaxation of 0.17%. The appearance of additional (200) diffraction component in asymmetric peak fitting of FS-BTO reflection is consistent with formation of a small fraction of (200) (or (020))

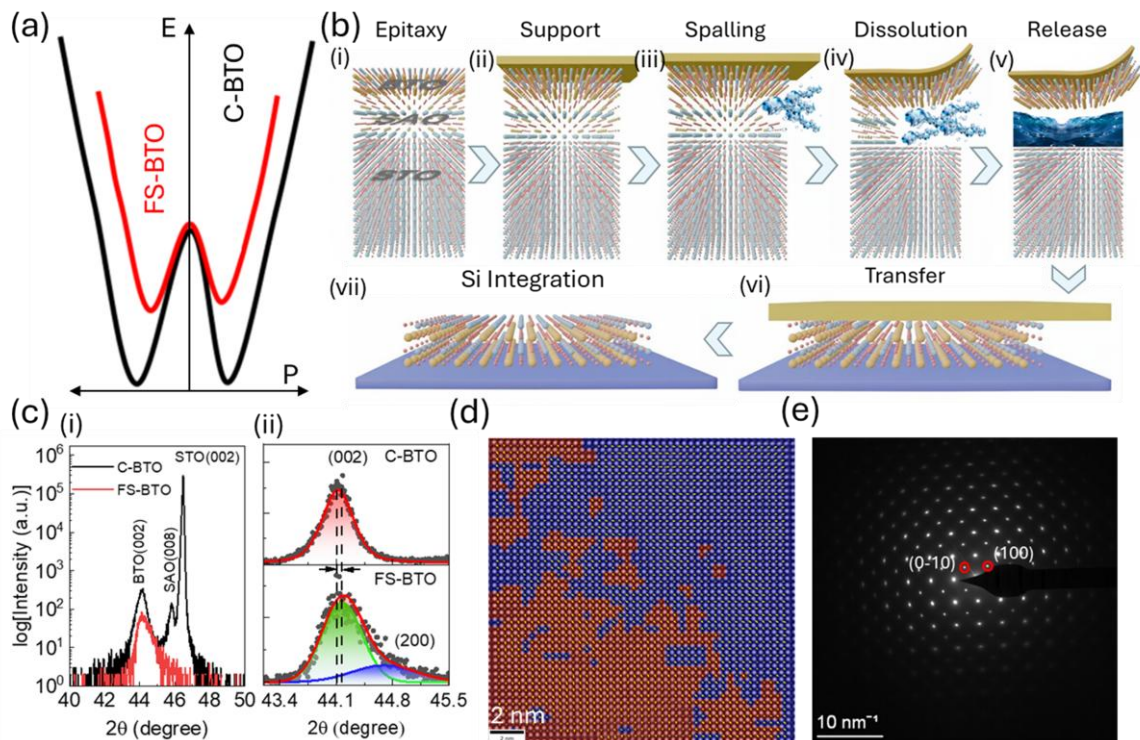


Figure 1. (a) Schematic illustration of de-clamping effect driven energy barrier modification in double well potential of C-BTO and FS-BTO membrane. (b) Schematic flow of the fabrication and transfer of FS-BTO involving steps of (i) epitaxy growth, (ii) attaching support layer, (iii) spalling, (iv) dissolution and (v) release in water followed by (vi) transfer on (vii) Si substrate. (c) XRD scan of (i) the epitaxial grown SAO/BTO stack (C-BTO) and BTO membrane (FS-BTO). (ii) Peak fitting of the BTO (002) reflection for strain relaxation and emergence of (200) planes in FS-BTO. (d) Polarization map of the HAADF-STEM with red and blue color marked region indicating in-plane domains. (e) SAED pattern of the BTO membrane from [001].

oriented ferroelastic domains due to strain relaxation. Plan view HAADF-STEM image (Figure 1d) of the transferred FS-BTO, along with corresponding polar-displacement vector maps, reveal in-plane domains ([100] and [010] oriented) (Figure S2). In addition, the selected-area electron diffraction pattern acquired from FS-BTO (Figure 1e) exhibits sharp, periodic diffraction spots indexed along the (100) zone axis, further confirming the single-crystalline nature of the transferred membrane. These observations are supported by Raman spectroscopy measurements, where the appearance of representative tetragonal phase BTO modes, i.e.,  $305\text{ cm}^{-1}$   $B_1/E(\text{TO}_3 + \text{LO}_2)$ ,  $525\text{ cm}^{-1}$   $A_1(\text{TO}_3)$  and  $715\text{ cm}^{-1}$   $A_1(\text{LO}_3)/E(\text{LO}_4)$ , confirms the intrinsic polar structure of the FS-BTO membrane (Figure S4).<sup>32, 33</sup>

To complement these structural results, we next investigate the surface morphology and local polar properties of FS-BTO membrane using piezoresponse force microscopy (PFM) and KPFM. AFM topography confirms a wrinkle and crack-free FS-BTO surface with a root-mean-square roughness of  $\sim 0.4\text{ nm}$  (Figure S5). Figure 2a displays the smooth surface of the FS-BTO membrane transferred to Si substrate with corresponding PFM phase and amplitude response shown in Figure 2(b, c). To investigate the ferroelectric domain switching, we conducted domain writing and erasing measurement with  $\pm 20\text{ V}$  biasing. The obtained  $180^\circ$  dipole orientation in the phase images confirms the intrinsic out-of-plane ferroelectricity in FS-

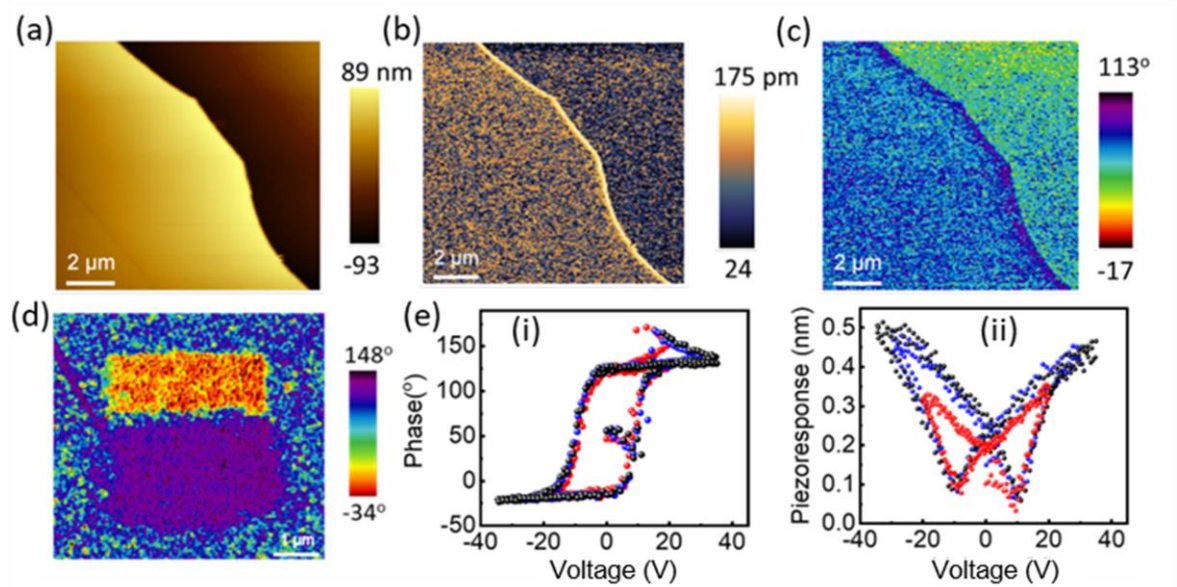


Figure 2. (a-c) AFM (a) topography, (b) amplitude and (c) phase image of the BTO membrane on Pt/Si substrate. (d) Ferroelectric domain writing and erasing with  $\pm 20\text{ V}$ . (e) DART mode PFM off field (i) phase and (ii) piezoresponse amplitude switching spectroscopy.

BTO membrane (Figure 2d).<sup>32</sup> Consistently, off-field PFM spectroscopy exhibits well-defined phase and piezoresponse hysteresis loops with a coercive voltage of  $\sim 10\text{ V}$  (Figure 2e(i,ii)),

validating the ferroelectric and piezoelectric nature of FS-BTO. With the given intrinsic polarization and clamping strain<sup>6</sup> free polarization dynamics, we examined the thermal sensitivity of the domains by mapping PFM phase and piezoresponse as a function of temperature at a fixed AC read voltage. Figure 3 summarizes the temperature-evolution of amplitude and phase of piezoresponse of specific representative region from 30°C to 50°C. At 30 °C, the piezo response amplitude and phase in region R1 correspond to 715 pm and 18°, respectively, and in region R2 they correspond to 538 pm and 202° respectively (Figure 3a(i,ii)). Phase response suggests that R1 and R2 are 180° domains (Figure 3b(i)), and in general the sample shows a bi-modal phase distribution centered around 18° and 202°. This observation of 180° oriented domains is consistent with previously reported 180° oriented super-domains in nearly free standing BTO lamella.<sup>34, 35</sup> Upon increasing the temperature to 40°C, the bimodal phase distribution still remains, however with a much-reduced phase difference of 10° (Figure 3b(ii) and Figure S6a) between the domains, with a decreased average amplitude of 592 pm (Figure 3c). At 50 °C, piezoresponse reduced further to  $\sim 507 \pm 10$  pm at 50°C as shown in

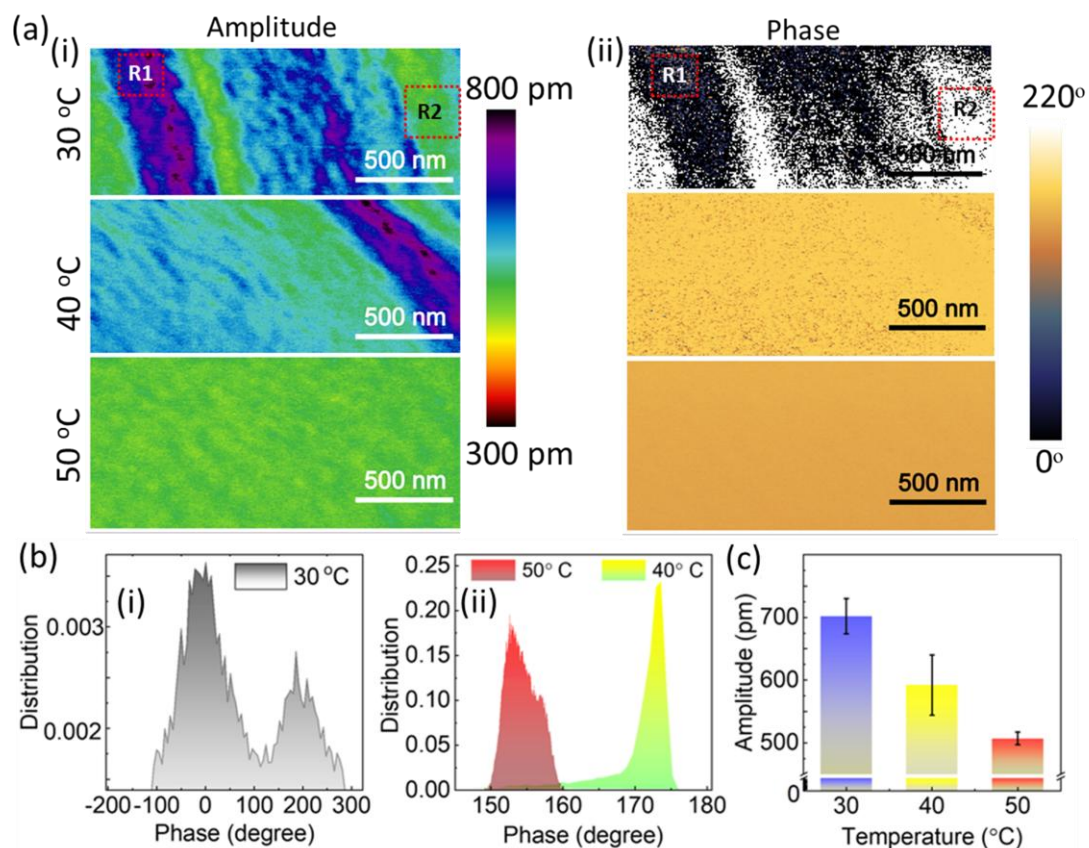


Figure 3. Temperature dependent (a) PFM (i) amplitude and (ii) phase images at 30, 40 and 50 °C from the same area. (b) Temperature-dependent evolution of the phase distribution from (i) bimodal (180°-oriented) at 30 °C to (ii) unimodal above 40 °C with increased full width half maxima indicating enhanced disorder of domains at 50 °C. (c) Statistical distribution of average piezo-response at different temperature.

Figure 3c, and a uni-modal distribution emerges (Figure 3b(ii) and Figure S6b)).<sup>36, 37</sup> These results are consistent with temperature sensitive polarization disordering and reorientation. Earlier works have reported periodicity doubling cascades with increasing temperature in ferroelastic BaTiO<sub>3</sub>, eventually resulting in complete disordering at the curie temperature.<sup>24</sup> Hence, the thermal sensitivity of the domains is attributed to the temperature induced polarization rotation and disordering.<sup>24</sup> Furthermore, reduced activation barriers in energy landscape in the epitaxial strain free membrane enhances the sensitivity of polar domain rotation to temperature, leading to measurable changes in dipolar orientation with small changes in temperature.<sup>24, 38</sup>

Having established intrinsic ferroelectricity and thermal sensitivity of polarization rotation, we next investigate the pyroelectric response of the FS-BTO membrane using temperature-dependent KPFM.<sup>39-41</sup> Figure 4a displays the schematic representation of KPFM measurement, where the tip scans the topography at fixed height and detects the surface potential after a lift of 50 nm. In KPFM, the measured surface potential corresponds to the contact potential difference,  $V_{CPD}$ , i.e., the DC bias applied to null the electrostatic force arising from the work-function difference between the tip and the sample (as illustrated in Figure 4b).<sup>42</sup> The tip work function was calibrated using highly oriented pyrolytic graphite (HOPG)<sup>42, 43</sup> after which the calibrated tip was used to acquire temperature-dependent KPFM maps across the membrane-substrate boundary. Figure 4c shows the  $\Delta V_{CPD}$  extracted from the data presented in Figure 4d. The step-like contrast in the topography indicates a membrane thickness of  $\sim 150$  nm. The corresponding KPFM profile indicates a clear temperature dependence of the surface potential, where the effective change in potential between top and bottom surface of the membrane,  $\Delta V_{CPD}$ , decreases with increasing temperature. The change in electrical displacement ( $D$ ) is related to the differential surface potential of the membrane through equation (2).<sup>44</sup>

$$\Delta D = \frac{\Delta V \varepsilon_0 \varepsilon_{BTO}}{d_{BTO}} \quad (2)$$

Where,  $\varepsilon_0$  is permittivity of free space,  $\varepsilon_{BTO}$  is relative permittivity of BTO,  $d_{BTO}$  is the thickness of membrane. Therefore, the nonlinear negative slope profile of the  $\Delta V_{CPD}$  with temperature is attributed to decrease in polarization of the ferroelectric membrane.

Under zero bias condition, temperature induced electric displacement leads to thermal modulation of spontaneous polarization that leads to pyroelectricity in FS-BTO membrane.<sup>41</sup> The effective pyroelectric coefficient ( $\pi$ ) of the membrane can be extracted by equation (3).

$$\pi = \frac{\Delta P_S}{\Delta T} = \frac{\Delta D}{\Delta T} \quad (3)$$

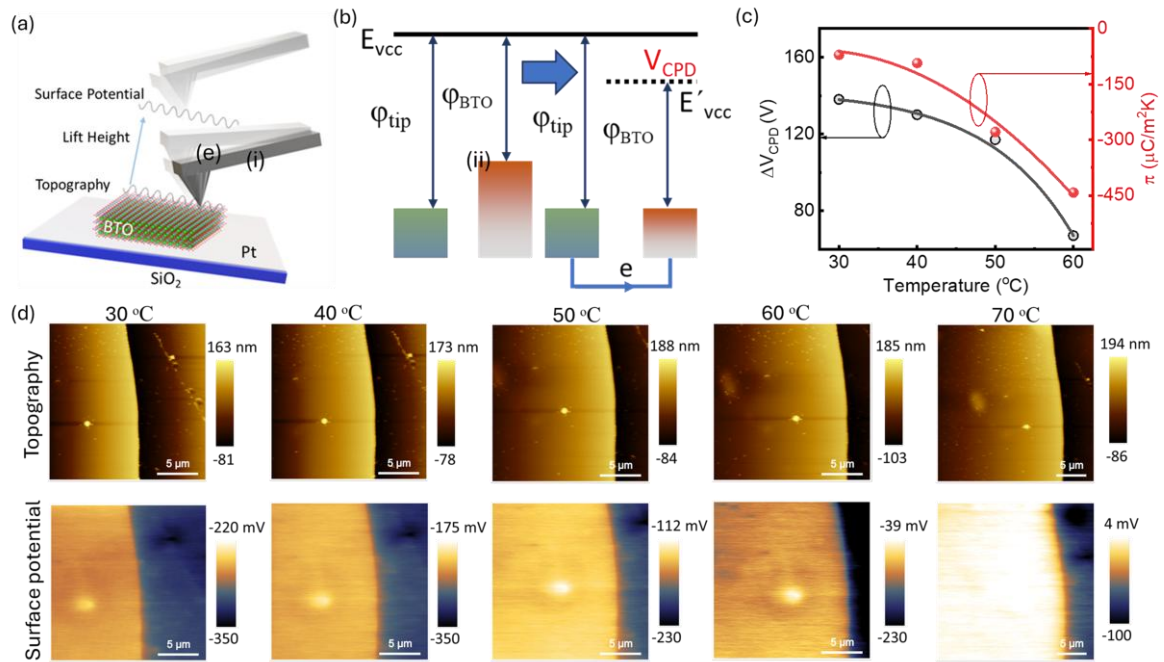


Figure 4. (a) Schematic representation of the KPFM measurement and (b) corresponding band diagram used for the contact surface potential analysis. (c–d) Variable-temperature (c) surface potential with the corresponding pyroelectric coefficient obtained from (d) simultaneous topography and surface potential measurements using KPFM.

The temperature-dependent surface potential,  $\Delta V_{CPD}(T)$ , obtained from KPFM was used to calculate the electric displacement and extract the effective pyroelectric coefficient  $\pi$  using equations (2) and (3). At RT, the observed pyroelectric coefficient in FS-BTO membrane is  $\sim 75 \mu C/m^2K$  (Figure 4c), which is nearly 7.5 times the bulk BTO and 4 times higher than 140 nm thin films of (clamped) BTO grown on a substrate (Figure 5a).<sup>45</sup> This magnitude of pyroelectricity increases with increase in temperature, and at 60 $^{\circ}C$  our FS-BTO membrane exhibits  $\pi$  of 450  $\mu C/m^2K$  (Figure 5b), which is  $\sim 34x$  of clamped thin film-based pyroelectrics.<sup>45-47</sup> The improved pyroelectricity in the free-standing membrane is attributed to de-clamping effect driven improved rotation of dipolar orientation, i.e., reconfiguration of dipoles in response to temperature change.<sup>19, 25, 27, 48</sup> The current study presents highest pyroelectric figure of merit ( $F_D$ ) of  $\sim 40 m^2C^{-1}$  in crystalline, lead-free oxide membranes, surpassing previously reported values in the literature, including CBNO-based 2D

quasicrystals at a comparable thickness of 150 nm, as shown in Figure 5c.<sup>19, 20</sup> Improved pyroelectric detectivity in lead-free freestanding oxide membranes supports their potential for on-chip (silicon-based) cryogen-free infrared sensing and waste-heat energy conversion. More broadly, coupling silicon integration with mechanical boundary-condition (strain/de-clamping) engineering provides a practical route to high-performance pyroelectric oxide devices.

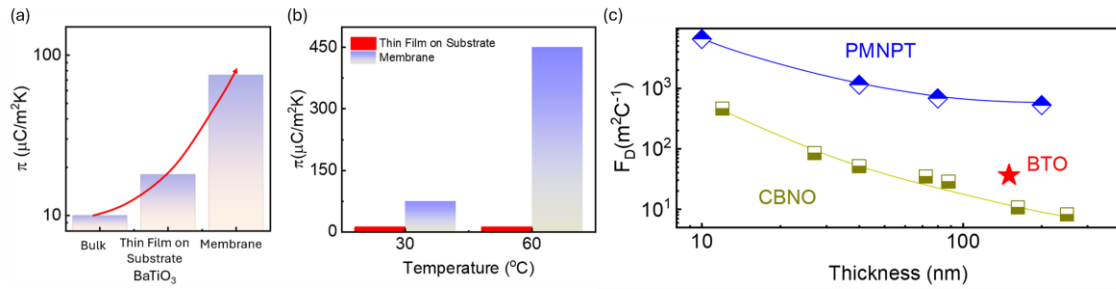


Figure 5. (a,b) Comparative analysis of the pyroelectric coefficient of bulk, thin film and FS-BTO membranes at 30°C and 60°C.<sup>45</sup> (c) Pyroelectric detectivity of the membranes from the literature.<sup>19, 20</sup>

In conclusion, we demonstrate de-clamping enabled strain engineering in FS-BTO membranes leads to an enhanced pyroelectric response, with an effective pyroelectric coefficient of  $\sim 75$   $\mu\text{C}/\text{m}^2\text{K}$  at 30°C and  $\sim 450$   $\mu\text{C}/\text{m}^2\text{K}$  at 60°C with  $F_D$  of  $\sim 40$   $\text{m}^2\text{C}^{-1}$ . Temperature-dependent PFM reveals a thermally driven evolution of the ferroelectric domain state, consistent with reduced barriers for small-angle dipolar reorientation in the freestanding geometry. Leveraging this enhanced thermal sensitivity, we have demonstrated 4 times higher pyroelectric coefficient in free standing membranes as compared to clamped thin films of BTO. These findings establish lead-free freestanding BTO membranes as a promising silicon-integrable platform for high-performance pyroelectric oxide electronics.

Supporting information file includes details of the characterization of the free-standing membranes.

## Methods:

### *Thin film deposition and transfer:*

Thin films were deposited by pulsed laser deposition (PLD) using a 248 nm excimer laser. Sacrificial SAO layers were grown on STO substrates at 850 °C, an oxygen partial pressure ( $P_{\text{O}_2}$ ) of  $2 \times 10^{-5}$  mbar, and a laser fluence of  $1.5 \text{ J cm}^{-2}$ . BaTiO<sub>3</sub> (BTO) films were subsequently deposited at 800 °C under  $P_{\text{O}_2}$  values of  $2 \times 10^{-5}$  mbar and  $5 \times 10^{-3}$  mbar with a laser fluence

of  $0.9 \text{ J cm}^{-2}$ . For membrane transfer, PMMA was first spin-coated onto the BTO/SAO//STO heterostructure. The samples were then immersed in room-temperature deionized water to dissolve the SAO sacrificial layer. The released BTO membrane was subsequently scooped onto a Si substrate, and the PMMA support layer was removed by dissolving it in acetone.

#### *AFM, PFM, KPFM measurements:*

The nano scale analysis for the topography and electrical properties analysis of the FS-BTO membrane was carried out by Oxford MFP 3D Origin+ system, where dual AC resonance tracking mode is employed to measure the PFM response. The temperature dependent surface potential analysis was performed by amplitude modulated KPFM measurements. All of the measurements were performed with Pt/Ir coated SCM-PIT-V2 conducting tips with spring constant of 3 N/m and resonance frequency of 75 kHz.

#### *Raman spectroscopy:*

Raman spectra were obtained using a Raman spectrometer (HORIBA JOBIN VYON make, 47 model LabRAM HR (UV) system) with a 532 nm laser excitation source.

#### *STEM HAADF imaging:*

Cross-sectional lamellae were prepared by focused ion-beam milling (FEI Scios 2). Aberration-corrected HAADF-STEM imaging was performed on a Titan Themis operated at 300 kV (probe convergence 24 mrad; HAADF collection 48-200 mrad). Atomic-resolution HAADF-STEM images were subsequently used for polar mapping by quantifying Ti cation displacements relative to the Ba (A-site) sublattice: distortion-free lattice images were Bragg-filtered in Digital Micrograph, and Ti column positions were analyzed using AtoMap and the Temul-toolkit to generate vector maps of the local unit-cell dipole moment in BTO.

#### **Notes**

The authors declare no competing financial interest.

#### **Author Information**

Corresponding Author

\*Pavan Nukala, Email : pnukala@iisc.ac.in

\*Ajay Kumar, Email: ajaykumar2@iisc.ac.in

\*Asraful Haque, Email : asrafulhaque@iisc.ac.in

## Acknowledgements

This work was partly carried out at the Micro and Nano Characterization Facility (MNCF), Advanced Facility for Microscopy and Microanalysis (AFMM) and National Nanofabrication Center (NNfC) located at IISc Bengaluru and benefitted from all the help and support from the staff. This work is supported by Anusandhan National Research Foundation (ANRF), government of India under grant number ANRF/ARG/2025/002959/ENS. A.H. would like to acknowledge Dr. Mehak Mehta and Prof. Sushobhan Avasthi for providing access to high-temperature PLD facilities.

## References

1. Bakaul, S. R.; Serrao, C. R.; Lee, M.; Yeung, C. W.; Sarker, A.; Hsu, S.-L.; Yadav, A. K.; Dedon, L.; You, L.; Khan, A. I.; Clarkson, J. D.; Hu, C.; Ramesh, R.; Salahuddin, S., Single crystal functional oxides on silicon. *Nat. Commun.* **2016**, *7*, 10547.
2. Wang, H.; Harbola, V.; Wu, Y.-J.; van Aken, P. A.; Mannhart, J. Interface Design beyond Epitaxy: Oxide Heterostructures Comprising Symmetry-Forbidden Interfaces. *Adv. Mater.* **2024**, *36*, 2405065.
3. Xu, R.; Huang, J.; Barnard, E. S.; Hong, S. S.; Singh, P.; Wong, E. K.; Jansen, T.; Harbola, V.; Xiao, J.; Wang, B. Y.; Crossley, S.; Lu, D.; Liu, S.; Hwang, H. Y., Strain-induced room-temperature ferroelectricity in SrTiO<sub>3</sub> membranes. *Nat. Commun.* **2020**, *11*, 3141.
4. Sheeraz, M.; Jung, M.-H.; Kim, Y. K.; Lee, N.-J.; Jeong, S.; Choi, J. S.; Jo, Y. J.; Cho, S.; Kim, I. W.; Kim, Y.-M.; Kim, S.; Ahn, C. W.; Yang, S. M.; Jeong, H. Y.; Kim, T. H. Freestanding Oxide Membranes for Epitaxial Ferroelectric Heterojunctions. *ACS Nano* **2023**, *17*, 13510-13521.
5. McKee, R. A.; Walker, F. J.; Chisholm, M. F., Crystalline Oxides on Silicon: The First Five Monolayers. *Phys. Rev. Lett.* **1998**, *81*, 3014-3017.
6. Lyu, J.; Fina, I.; Solanas, R.; Fontcuberta, J.; Sánchez, F., Tailoring Lattice Strain and Ferroelectric Polarization of Epitaxial BaTiO<sub>3</sub> Thin Films on Si(001). *Sci. Rep.* **2018**, *8*, 495.
7. Haque, A.; Mandal, S. K.; Parate, S. K.; D'souza, H. J.; Nukala, P.; Raghavan, S., Free standing epitaxial oxides through remote epitaxy: the role of the evolving graphene microstructure. *Nanoscale* **2025**, *17*, 2020-2031.

8. Haque, A.; Mandal, S. K.; Jeyaseelan, A.; Vura, S.; Nukala, P.; Raghavan, S., Remote epitaxy-based atmospherically stable hybrid graphene template for fast and versatile transfer of complex ferroelectric oxides onto Si, *Mater. Today* **2024**, 8, 100091.
9. Mandal, R.; Yun, S.; Wurster, K.; Dollekamp, E.; Shondo, J. N.; Pryds, N., Recent Advancement in Ferroic Freestanding Oxide Nanomembranes. *Nano Lett.* **2025**, 25, 5541-5549.
10. Kum, H. S.; Lee, H.; Kim, S.; Lindemann, S.; Kong, W.; Qiao, K.; Chen, P.; Irwin, J.; Lee, J. H.; Xie, S.; Subramanian, S.; Shim, J.; Bae, S.-H.; Choi, C.; Ranno, L.; Seo, S.; Lee, S.; Bauer, J.; Li, H.; Lee, K.; Robinson, J. A.; Ross, C. A.; Schlom, D. G.; Rzechowski, M. S.; Eom, C.-B.; Kim, J., Heterogeneous integration of single-crystalline complex-oxide membranes, *Nature* **2020**, 578, 75-81.
11. Hu, Y.; Yang, J.; Liu, S., Giant piezoelectric effects of topological structures in stretched ferroelectric membranes. *Phys. Rev. Lett.* **2024**, 133, 046802.
12. Kondovych, S.; Boron, L.; Di Rino, F. N.; Sepliarsky, M.; Razumnaya, A. G.; Sené, A.; Lukyanchuk, I. A., Surface-tension-induced phase transitions in freestanding ferroelectric thin films, *Nano Lett.* **2025**, 25, 12987-12994.
13. Shi, Q.; Parsonnet, E.; Cheng, X.; Fedorova, N.; Peng, R.-C.; Fernandez, A.; Qualls, A.; Huang, X.; Chang, X.; Zhang, H.; Pesquera, D.; Das, S.; Nikonov, D.; Young, I.; Chen, L.-Q.; Martin, L. W.; Huang, Y.-L.; Íñiguez, J.; Ramesh, R., The role of lattice dynamics in ferroelectric switching. *Nat. Commun.* **2022**, 13, 1110.
14. Paul, M., Micromachined infrared detectors based on pyroelectric thin films, *Rep. Prog. Phys.* **2001**, 64, 1339.
15. Whatmore, R. W., Pyroelectric devices and materials, *Rep. Prog. Phys.* **1986**, 49, 1335.
16. Pandya, S.; Velarde, G.; Zhang, L.; Wilbur, J. D.; Smith, A.; Hanrahan, B.; Dames, C.; Martin, L. W., New approach to waste-heat energy harvesting: pyroelectric energy conversion. *NPG Asia Mater.* **2019**, 11, 26.
17. Szigeti, B., Temperature dependence of pyroelectricity *Phys. Rev. Lett.* **1975**, 35, 1532-1534.
18. Velarde, G.; Pandya, S.; Karthik, J.; Pesquera, D.; Martin, L. W., Pyroelectric thin films—Past, present, and future. *APL Mater.* **2021**, 9, 1.
19. Jiang, J.; Zhang, L.; Ming, C.; Zhou, H.; Bose, P.; Guo, Y.; Hu, Y.; Wang, B.; Chen, Z.; Jia, R.; Pendse, S.; Xiang, Y.; Xia, Y.; Lu, Z.; Wen, X.; Cai, Y.; Sun, C.; Wang, G.-C.; Lu, T.-M.; Gall, D.; Sun, Y.-Y.; Koratkar, N.; Fohtung, E.; Shi, Y.; Shi, J., Giant pyroelectricity in nanomembranes. *Nature* **2022**, 607, 480-485.

20. Zhang, X.; Ericksen, O.; Lee, S.; Akl, M.; Song, M.-K.; Lan, H.; Pal, P.; Suh, J. M.; Lindemann, S.; Ryu, J.-E.; Shao, Y.; Zheng, X.; Han, N. M.; Bhatia, B.; Kim, H.; Kum, H. S.; Chang, C. S.; Shi, Y.; Eom, C.-B.; Kim, J., Atomic lift-off of epitaxial membranes for cooling-free infrared detection. *Nature* **2025**, 641, 98-105.
21. Lin, C.-C.; Hu, Y.; Kim, J.; Lou, D.; Bhat, A.; Kavle, P.; Kim, T. Y.; Dames, C.; Liu, S.; Martin, L. W., Domain-wall enhanced pyroelectricity. *Phys. Rev. X* **2025**, 15, 011063.
22. Gong, H.; Zhang, Y.; Zatterin, E.; Zhou, X.; Xiang, S.; Jiang, T.; Wang, Q.; Zhou, X.; Zhou, X.; Hu, Y.; Molina-Luna, L.; Xu, B.-X.; Zhuo, F.; Wu, H.-H.; Zhang, D.; Bowen, C., Dislocation-Enhanced Pyroelectricity in Barium Titanate. *Adv. Mater.* **2025**, n/a, (n/a), e15988.
23. Li, Y. L.; Cross, L. E.; Chen, L. Q., A phenomenological thermodynamic potential for BaTiO<sub>3</sub> single crystals. *J. Appl. Phys.* **2005**, 98, 6.
24. Everhardt, A. S.; Damerio, S.; Zorn, J. A.; Zhou, S.; Domingo, N.; Catalan, G.; Salje, E. K. H.; Chen, L.-Q.; Noheda, B., Periodicity-doubling cascades: direct observation in ferroelastic materials. *Phys. Rev. Lett.* **2019**, 123, 087603.
25. Dong, G.; Li, S.; Yao, M.; Zhou, Z.; Zhang, Y.-Q.; Han, X.; Luo, Z.; Yao, J.; Peng, B.; Hu, Z.; Huang, H.; Jia, T.; Li, J.; Ren, W.; Ye, Z.-G.; Ding, X.; Sun, J.; Nan, C.-W.; Chen, L.-Q.; Li, J.; Liu, M., Super-elastic ferroelectric single-crystal membrane with continuous electric dipole rotation. *Science* **2019**, 366, 475-479.
26. Zhang, X.; Lee, S.; Ryu, J.-E.; Suh, J. M.; Kim, T.-H.; Barone, M. R.; Parker, N. A.; Lee, G.; Kim, I.-J.; Yeo, I.; Shin, J.; Lee, J.-S.; Schlom, D. G.; Chang, C. S.; Seo, J.-s.; Yu, S.; Song, M.-K.; Kim, J., Single-crystalline BaTiO<sub>3</sub>-based ferroelectric capacitive memory via membrane transfer. *Sci. Adv.* 11, eadz2553.
27. Pal, S.; Hsu, L.-T.; Sun, H.; Teng, S.-H.; Dwij, V.; Palladino, E.; Nie, Y.; John, S.; Prabhu, S. S.; Grünebohm, A.; Briscoe, J., Subsecond optically controlled domain switching in freestanding ferroelectric BaTiO<sub>3</sub> membrane. *Nat. Commun.* **2025**, 16, 7940.
28. Adkins, J. W.; Fina, I.; Sánchez, F.; Bakaul, S. R.; Abiade, J. T., Polarization-dependent electrocaloric and pyroelectric effects in ferroelectric BaTiO<sub>3</sub> thin films. *Appl. Phys. Lett.* **2023**, 122, 10.
29. Lyahovitskaya, V.; Zon, I.; Feldman, Y.; Cohen, S.; Lubomirsky, I., Non-crystalline pyroelectric BaTiO<sub>3</sub> thin films. *Mater. Sci and Eng.: B* **2004**, 109, 167-169.

30. Ivry, Y.; Lyahovitskaya, V.; Zon, I.; Lubomirsky, I.; Wachtel, E.; Roytburd, A. L., Enhanced pyroelectric effect in self-supported films of BaTiO<sub>3</sub> with polycrystalline macrodomains. *Appl. Phys. Lett.* **2007**, 90, 17.
31. Haque, A.; D'Souza, H. J.; Parate, S. K.; Sandilya, R. S.; Raghavan, S.; Nukala, P., Heterogeneous Integration of High Endurance Ferroelectric and Piezoelectric Epitaxial BaTiO<sub>3</sub> Devices on Si. *Adv. Funct. Mater.* **2025**, 35, 2413515.
32. Choo, S.; Varshney, S.; Shah, J.; Manjeshwar, A. K.; Lee, D. K.; Mkhoyan, K. A.; James, R. D.; Jalan, B., Hybrid MBE Route to Adsorption-Controlled Growth of BaTiO<sub>3</sub> Membranes with Robust Polarization Switching. *Nano Lett.* **2025**.
33. Dwij, V.; De, B. K.; Sharma, G.; Shukla, D. K.; Gupta, M. K.; Mittal, R.; Sathe, V., Revisiting eigen displacements of tetragonal BaTiO<sub>3</sub>: Combined first principle and experimental investigation. *Physica B: Condens. Matter* **2022**, 624, 413381.
34. McGilly, L. J.; Gregg, J. M., Scaling of superdomain bands in ferroelectric dots. *Appl. Phys. Lett.* **2011**, 98, 132902.
35. Schilling, A.; Byrne, D.; Catalan, G.; Webber, K. G.; Genenko, Y. A.; Wu, G. S.; Scott, J. F.; Gregg, J. M., Domains in ferroelectric nanodots. *Nano Lett.* **2009**, 9, 3359-3364.
36. Walker, J.; Ursic, H.; Bencan, A.; Malic, B.; Simons, H.; Reaney, I.; Viola, G.; Nagarajan, V.; Rojac, T., Temperature dependent piezoelectric response and strain–electric-field hysteresis of rare-earth modified bismuth ferrite ceramics. *J. Mater. Chem. C* **2016**, 4, 7859-7868.
37. Yuan, G.; Chen, J.; Xia, H.; Liu, J.; Yin, J.; Liu, Z., Ferroelectric domain evolution with temperature in BaTiO<sub>3</sub> film on (001) SrTiO<sub>3</sub> substrate. *Appl. Phys. Lett.* **2013**, 103, 062903.
38. Koukhar, V. G.; Pertsev, N. A.; Waser, R., Thermodynamic theory of epitaxial ferroelectric thin films with dense domain structures. *Phys. Rev. B* **2001**, 64, 214103.
39. Niu, L.; Liu, F.; Zeng, Q.; Zhu, X.; Wang, Y.; Yu, P.; Shi, J.; Lin, J.; Zhou, J.; Fu, Q.; Zhou, W.; Yu, T.; Liu, X.; Liu, Z., Controlled synthesis and room-temperature pyroelectricity of CuInP<sub>2</sub>S<sub>6</sub> ultrathin flakes. *Nano Energy* **2019**, 58, 596-603.
40. Cuniot-Ponsard, M., Kelvin probe force microscopy and electrostatic force microscopy responses to the polarization in a ferroelectric thin film: Theoretical and experimental investigations. *J. Appl. Phys.* **2013**, 114, 014302.
41. McCluskey, C. J.; Sharma, N.; Maguire, J. R.; Pauly, S.; Rogers, A.; Lindsay, T. J.; Holsgrove, K. M.; Rodriguez, B. J.; Soin, N.; Gregg, J. M.; McQuaid, R. G. P.; Kumar,

- A., Spatially resolved high voltage Kelvin probe force microscopy: a novel avenue for examining electrical phenomena at nanoscale. *Adv. Phys. Res.* **2024**, 3, 2400011.
42. Kumar, A.; Mandal, D., Control of intrinsic polarity for work function modulation of polyvinylidene fluoride crystalline phases. *Appl. Phys. Lett.* **2023**, 123, 121603.
43. Zahmatkeshsaredorahi, A.; Jakob, D. S.; Xu, X. G., Pulsed Force Kelvin Probe Force Microscopy— A New Type of Kelvin Probe Force Microscopy under Ambient Conditions. *J. Phys. Chem. C* **2024**, 128, 9813-9827.
44. Belianinov, A.; He, Q.; Dziaugys, A.; Maksymovych, P.; Eliseev, E.; Borisevich, A.; Morozovska, A.; Banys, J.; Vysochanskii, Y.; Kalinin, S. V., CuInP2S6 Room Temperature Layered Ferroelectric. *Nano Letters* **2015**, 15, 3808-3814.
45. Li, H.; Bowen, C. R.; Dan, H.; Yang, Y., Pyroelectricity induced by Schottky interface above the Curie temperature of bulk materials. *Joule* **2024**, 8, 401-415.
46. Varan, A. H.; Yaman, M. F.; Öztürk, Z. Z.; Büyükköse, S.; Berber, S.; Seyidov, M. Y., Employing the pyroelectric effect in LiTaO<sub>3</sub> thin film for infrared detection of complex gases, *Mater. Res. Express* **2024**, 11, 125901.
47. Karthik, J.; Agar, J. C.; Damodaran, A. R.; Martin, L. W., Effect of 90° Domain Walls and Thermal Expansion Mismatch on the Pyroelectric Properties of Epitaxial PbZr<sub>0.2</sub>Ti<sub>0.8</sub>O<sub>3</sub> Thin Films *Phys. Rev. Lett.* **2012**, 109, 257602.
48. Sun, H.; Gu, J.; Li, Y.; Paudel, T. R.; Liu, D.; Wang, J.; Zang, Y.; Gu, C.; Yang, J.; Sun, W.; Gu, Z.; Tsymbal, E. Y.; Liu, J.; Huang, H.; Wu, D.; Nie, Y., Prominent size effects without a depolarization field observed in ultrathin ferroelectric oxide membranes. *Phys. Rev. Lett.* **2023**, 130, 126801.

## Supporting Information

# Large Pyroelectric Enhancement in Freestanding Epitaxial BaTiO<sub>3</sub> Membranes on Si

Ajay Kumar<sup>#\*</sup>, Asrafal Haque<sup>#\*</sup>, Shubham Kumar Parate, Harshal D'Souza, Jishnu NK, Binoy Krishna De, Srinivasan Raghavan, Pavan Nukala<sup>\*</sup>

Centre for Nano Science and Engineering, Indian Institute of Science, Bangalore 560012, India

<sup>#</sup> equal contribution

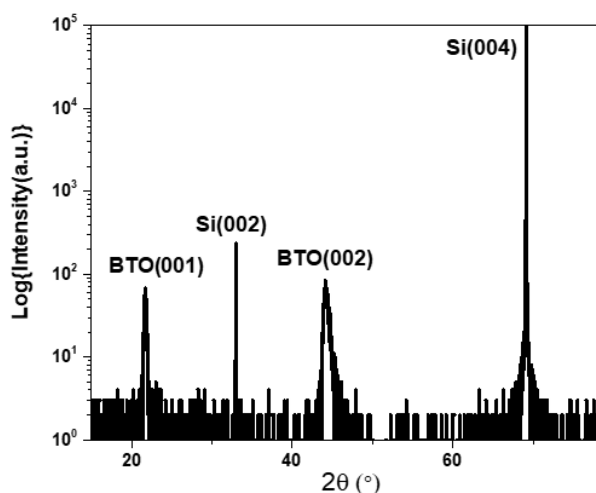


Figure S1. XRD of the single crystalline FS-BTO membrane transferred on Si.

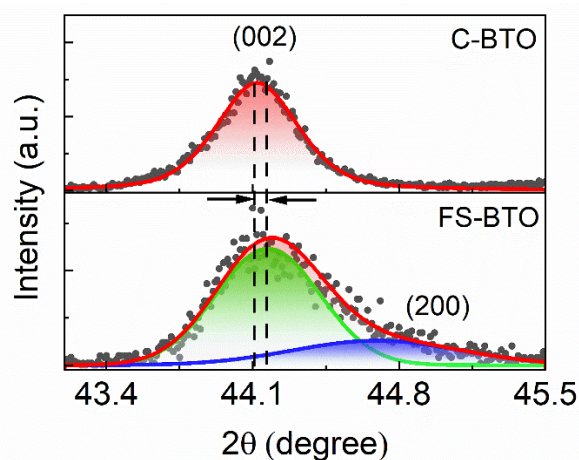


Figure S2. Fitted XRD (002) and (200) peaks of C-BTO and FS-BTO Membrane.

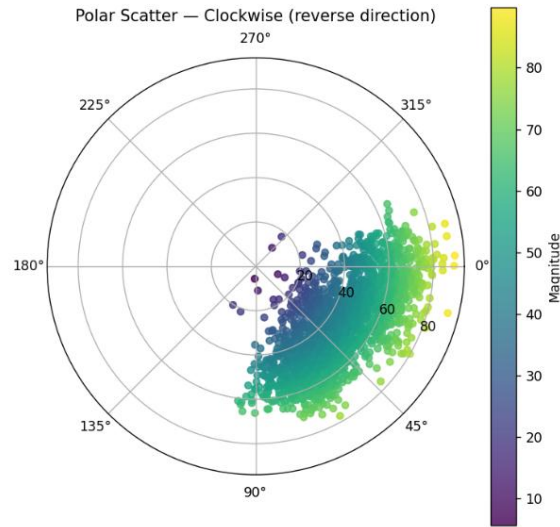


Figure S3. Polar plot of the polarisation vector from HAADF-STEM image of the BTO membrane.

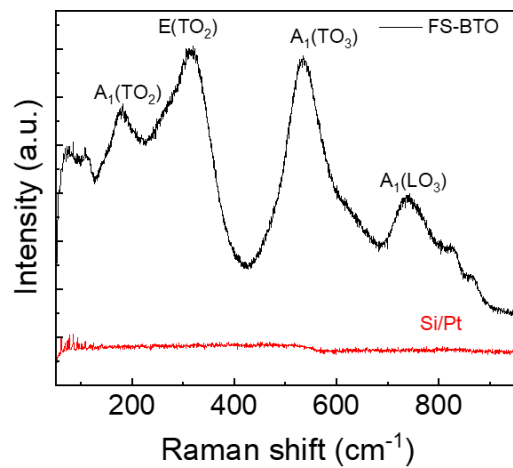


Figure S4. Raman spectra of the BTO membrane on Si/Pt substrate. Bare Si/Pt substrate Raman spectrum (red) is also presented for comparison.

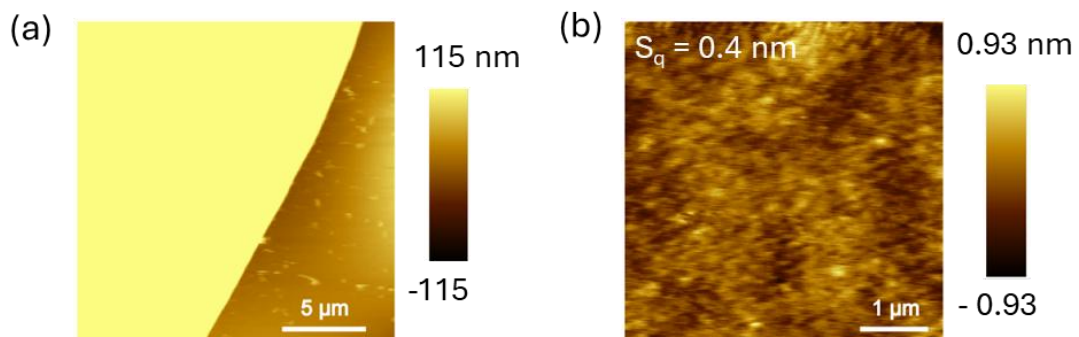


Figure S5. AFM of the (a) as transferred BTO membrane on Si substrate with corresponding (b) topography measurement from the top surface.

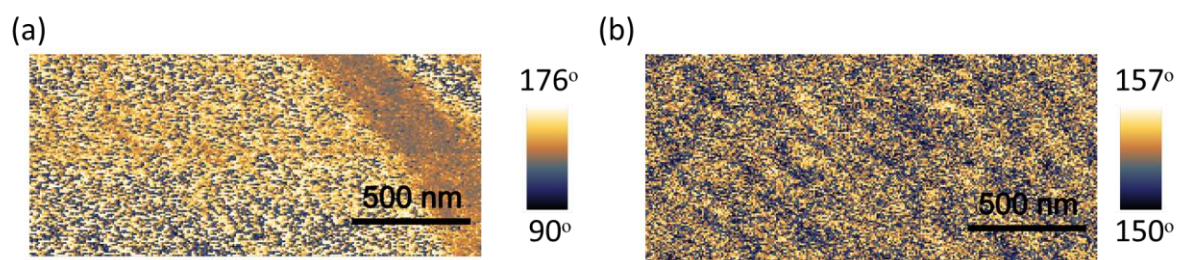


Figure S6. Temperature-dependent evolution of the phase distribution showing (a) a bimodal distribution with a phase difference of  $\sim 10^\circ$  at 40 °C, reduced from  $\sim 180^\circ$  at 30 °C, and (b) a unimodal phase distribution at 50 °C.